Heliyon 9 (2023) e15711

Contents lists available at ScienceDirect

Heliyon

journal homepage: www.cell.com/heliyon

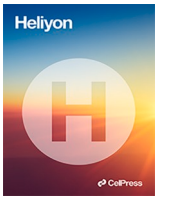

Research article

Assessing the effect of manufacturing defects and non-Newtonian blood model on flow behaviors of additively manufactured Gyroid TPMS structures

Saran Seehanam [a], Wares Chanchareon [b], Patcharapit Promoppatum [a,*]

[a] Center for Lightweight Materials, Design, and Manufacturing, Department of Mechanical Engineering, Faculty of Engineering, King Mongkut's University of Technology Thonburi (KMUTT), Bangmod, Bangkok, 10140, Thailand
[b] Princess Srisavangavadhana College of Medicine, Chulabhorn Royal Academy, Bangkok, 10210, Thailand

ARTICLE INFO

Keywords:
Additive manufacturing
Computational fluid dynamics
Laser powder bed fusion process
Triply periodic minimal surface
Non-Newtonian fluids

ABSTRACT

In the field of medical engineering, Triply Periodic Minimal Surfaces (TPMS) structures have been studied widely owing to their physical attributes similar to those of human bones. Computational Fluid Dynamics (CFD) is often used to reveal the interaction between structural architectures and flow fields. Nevertheless, a comprehensive study on the effect of manufacturing defects and non-Newtonian behavior on the fluid responses in TPMS scaffolds is still lacking. Therefore, the present study fabricated Gyroid TPMS with four relative densities from 0.1 to 0.4. Non-destructive techniques were used to examine surface roughness and geometric deviation. We found that the manufacturing defects had a minor effect on fluid responses. The pressure drop comparison between defect-containing and defect-free models could be differed up to 7%. The same comparison for the average shear stress showed a difference up to 23%, in which greater deviation between both models was observed at higher relative density. On the contrary, the viscosity model played a significant role in flow prediction. By comparing the Newtonian model with Carreau-Yasuda non-Newtonian model, the resulting pressure drop and average wall shear stress from non-Newtonian viscosity could be higher than those of the Newtonian model by more than a factor of two. In addition, we matched the fluid-induced shear stress from both viscosity models with desirable ranges of shear stresses for tissue growth obtained from the literature. Up to 70% from the Newtonian model fell within the desirable range while the matching stress reduced to lower than 8% for the non-Newtonian results. Furthermore, by correlating geometric features with physical outputs, the geometric deviation was seen associated with surface curvature while the local shear stress revealed a strong correlation with inclination angle. Overall, the present work emphasized the importance of the viscosity model for CFD analysis of the scaffolds, especially when resulting fluid-induced wall shear stress is of interest. In addition, the geometric correlation has introduced the alternative consideration of structural architectures from local perspectives, which could assist the further comparison and optimization among different porous scaffolds in the future.

* Corresponding author.
E-mail address: patcharapit.pro@kmutt.ac.th (P. Promoppatum).

https://doi.org/10.1016/j.heliyon.2023.e15711
Received 12 October 2022; Received in revised form 13 April 2023; Accepted 19 April 2023
Available online 25 April 2023

1. Introduction

A laser powder bed fusion (LPBF) process is among the most widely used Additive Manufacturing (AM) techniques [1]. It allows the formation of complex geometries that are difficult or even cannot be formed by traditional manufacturing processes. The LPBF technique applies the laser heat source to melt a thin layer of metal powders [2]. The combination of multiple melted layers enables the fabrication of a highly complex three-dimensional object. With such an advantage, the LPBF technique has been adopted greatly in the field of medical engineering [3]. Using the AM to fabricate implants enables the complex architectural design which could increase biocompatibility and proliferation of cell tissues [4]. Presently, the internal structures of metal implants have been integrated with cellular structures with 50–90% porosity [5]. Among many types of cellular structures, the Triply Periodic Minimal Surface (TPMS) structures have been regarded as a new class of geometry that provides favorable structural and biological responses. For this reason, the TPMS structures have drawn great attention as bone scaffolds [6]. A distinct characteristic of the TPMS structure lies in its mathematical-based formulation, in which important features such as pore size, unit cell size, and local relative density can be controlled precisely [7]. The nature of the TPMS structure exhibits zero-mean curvature at every local point. However, the Gaussian curvature can be non-zero and is adjustable by changing the types of structures or unit cell size. Among many types of TPMS structures, Gyroid was manufactured successfully and demonstrated favorable mechanical responses, illustrating its potential as a bone replacement architecture [8].

To date, researchers have explored the performance of the Gyroid as bone scaffolds using in-vivo, in-vitro, and in-silico approaches [9–13]. For instance, Ali et al. performed CFD analysis for several TPMS scaffolds including Gyroid, FRD, Primitive, and Diamond [9]. Gyroid provided the highest fluid permeability among the four structures which implied better nutrient transport through the scaffolds. Nonetheless, Ali et al. also noted the difficulty in correlating wall shear stress distribution with scaffold architectures. In addition, Ma et al. fabricated the Gyroid scaffolds using the LPBF techniques, in which the effect of design variables on mechanical properties, fluid transport, and biocompatibility was evaluated [10]. Overall, Gyroid scaffolds showed satisfactory biocompatibility, partly due to their large surface area and high fluid permeability. However, since Ma et al. utilized the CAD model for numerical simulation, they hypothesized that manufacturing defects such as surface roughness may affect the accuracy of mechanical and flow simulation. Moreover, Zou et al. also reported the in-vitro study which confirmed the bio-suitability of TPMS-based scaffolds [11]. In addition, Shi et al. [12] and Li et al. [13] have shown the significance of gradient TPMS scaffolds for enhancing biological responses. Shi et al. performed a CT scan of a rabbit femoral bone, in which the gradient TPMS scaffolds showed their engineerability to match morphological features and mechanical stiffness of natural bones [12]. Li et al., on the other hand, performed an in-vivo study. The graded scaffolds were shown to stimulate bone formation, and the early osseointegration of the TPMS-based scaffolds was confirmed [13].

Although the initial success of TPMS scaffolds for medical implants was evident, recent studies have shown that further design enhancement was feasible. Poltue et al. pointed out that TPMS assessment as medical implants was mostly focused on global responses such as effective elastic modulus, fluid permeability, and overall relative density [14]. Nonetheless, cell proliferation can also react to local stimuli such as fluid-induced shear stress [15]. Therefore, considering both global and local responses could lead to an internal structure with superior biological performance. In this regard, a high-fidelity CFD simulation can be a great design asset. Although several previous studies have utilized the CFD simulation to estimate the fluid-induced wall shear stress, there still exist some limitations. Firstly, the CFD simulation was often performed on a 3D CAD model [7,9,14]. However, LPBF parts may contain manufacturing defects such as surface roughness and geometrical deviation [16,17]. An investigation of manufacturing defects can be carried out using micro-computed tomography (micro-CT), where defects are frequently classified into internal and external ones [18]. Internal defects are voids inside printed structures while external defects may refer to either surface roughness or geometric deviation [17]. For surface roughness, digital microscopy can be an alternative examination method [19]. In solid mechanics, the results from micro-CT can be used to generate a defect-containing model, where simulated responses may reveal the influence of different defects on mechanical properties [17,20]. Even though the comparison between defect-containing and defect-free models was carried out widely for mechanical simulation, a similar comparison from a flow perspective is rarely seen.

Secondly, many previous studies on CFD simulation of scaffolds assumed Newtonian viscosity as previously seen in Poltue et al. [14], Pires et al. [21], and Montazerian et al. [22]. However, human blood, which contains red cells, white cells, platelets, and plasma, exhibits the rheological behavior of non-Newtonian fluid [23]. In a numerical framework, Fedosov et al. showed that the coarse-grained molecular dynamics could predict accurately the rate-dependent blood viscosity [24]. Such a model can reveal the interaction of red blood cells and their impact on blood rheology. Nonetheless, due to the difference in spatial and temporal scales, it is computationally challenging to apply a small-scale molecular dynamic framework to simulate the blood flow in vessels and medical scaffolds. Instead, phenomenological models were proposed, in which the blood viscosity is prescribed as a function of shear rate based on test results. Presently, several constitutive equations were developed including Carreau-Yasuda [25], Casson [26], Herschel-Bulkley [27], and power law models [28]. Even though phenomenological blood viscosity models were adopted widely in the CFD simulation of blood flow in arteries as seen in Johnson et al. [29], Yan et al. [30], and Zaman et al. [31], the study on the non-Newtonian effect on bone scaffolds design is very few. Mahammod et al. considered the non-Newtonian effect using the power law model on hydroxyapatite-based scaffolds [32]. Only the resulting pressure drop was analyzed, where the use of non-Newtonian fluid led to a larger pressure drop compared to that of Newtonian one. Furthermore, the non-Newtonian effect of TPMS scaffolds was carried out by Ali and Sen [33]. Similar to the results from Mahammod et al. [32], Ali and Sen [33] reported that the average shear stress and pressure drop of the non-Newtonian model were much larger than those of Newtonian models. However, it should be noted that Mahammod et al. [32] and Ali and Sen [33] focused mainly on assessing global responses such as pressure drop and average shear stress. The local distribution of resulting shear stress between Newtonian and non-Newtonian models was not comprehensively addressed. This issue is

of importance since cells respond to both global and local stimuli. In addition, when addressing the non-Newtonian effect, CAD models were used for the numerical simulation in previous works. Thus, although a comparison between Newtonian and non-Newtonian models has been carried out as seen in Mahammod et al. [32] and Ali and Sen [33], the competing influence between manufacturing defects and viscosity model for a fluid flow in the TPMS scaffolds has not been fully evaluated.

Therefore, the present study aimed to reveal the effect of manufacturing defects and viscosity models on the flow behavior of TPMS-based scaffolds. Gyroid TPMS was chosen in this work due to its prospective as a bone replacement structure. Several Gyroids with relative densities from 0.1 to 0.4 were made using the LPBF process. Surface morphologies and printed volumes were assessed for the manufacturability of Gyroid-based scaffolds. Based on the micro-CT data, defect-containing Gyroid models would be re-constructed for the CFD simulation. In addition, the non-Newtonian blood viscosity model would be implemented for comparison with the Newtonian-based results. Followingly, the CFD analyses would be performed to determine velocity profile, pressure drop, and fluid-induced wall shear stress. The influence of surface defects and viscosity models would be thoroughly examined from a perspective of a scaffold design and biological compatibility. Lastly, the correlation between geometrical features and outputs such as surface defects and local shear stresses would be evaluated. The physical correlation would provide insight into the controlling features of the Gyroids on their manufacturability and fluid behaviors. This understanding would assist in further development and optimization of the TPMS-based bone scaffolds.

2. Numerical models

2.1. Gyroid model

Triply Periodic Minimal Surface (TPMS) is categorized as surface-based lattice structures, which exhibit zero-mean curvature at every local point on their surfaces [34]. Even though many TPMS structures were examined for their physical responses in the literature, Gyroid is among the most widely used ones for bone implant application [35,36]. The nodal surface of the Gyroid could be formulated by solving Eq. (1). According to Eq. (1), 'L' represents the unit cell size. 'c' defines the level-set parameter, which can alter to adjust the shape of the Gyroid surface. To create the solid Gyroid, two surfaces with positive and negative 'c' are created, where the enclosed volume between two surfaces defines a sheet-based Gyroid solid. The present work utilized the MSLattice software to create the solid Gyroid with relative densities between 0.1 and 0.4 as shown in Fig. 1a [37]. Referring to Fig. 1a, the Gyroid solid was constructed with a 4 × 4 x 4 configuration and with a constant L of 5 mm. Therefore, the sample size (L_{sample}) is 20 × 20 × 20 mm^3, where a designated relative density was achieved by changing the sheet thickness by varying 'c' values. With the relative density of 0.1, 0.2, 0.3, and 0.4, the equivalent thicknesses of the Gyroid are 0.16, 0.32, 0.49, and 0.65 mm, respectively.

$$f(x,y,z) = \sin\left(\frac{2\pi}{L}x\right)cos\left(\frac{2\pi}{L}y\right) + sin\left(\frac{2\pi}{L}y\right)cos\left(\frac{2\pi}{L}z\right) + \sin\left(\frac{2\pi}{L}z\right)cos\left(\frac{2\pi}{L}x\right) = c \quad (1)$$

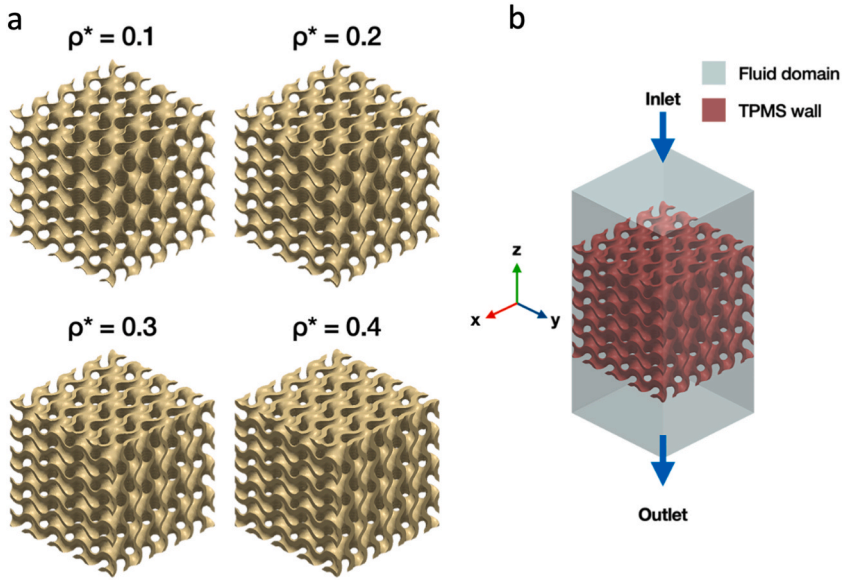

Fig. 1. a) Sheet-based Gyroid models with relative densities of 0.1, 0.2, 0.3 and 0.4 and b) Computational domain and boundary conditions for CFD analysis. The sample size is 20 × 20 × 20 mm^3.

2.2. Governing equation and boundary conditions

Navier-Stokes equation, formulated by mass and momentum conservations as seen in Eq. (2), was solved to obtain the fluid behaviors through the Gyroid scaffold. Fig. 1b illustrated the computational domain and boundary conditions adopted in the present work. An inlet velocity of 0.5 mm/s was chosen according to the blood flow from computational and experimental studies [33,38]. The zero-gauge pressure was defined at the outlet. Solid walls were defined with non-slip conditions while the fluid domain walls are specified with symmetry. Blood density was assumed to be 1050 kg/m^3. The CFD analysis was performed using COMSOL Multiphysics software under the steady state condition. In addition to the flow fields, the pressure drop and fluid-induced wall shear are the parameters of the interest in the present work. According to Darcy's law, the pressure drop could be used to determine the intrinsic fluid permeability of porous media using Eq. (3) [39]. Higher permeability indicates better nutrient transport in the scaffolds. On the other hand, the shear stress, determined from Eq. (4), can provide the mechanical stimuli for tissue growth and proliferation. In addition, the effect of domain size, mesh sensitivity study, and numerical model validation have been included in Appendix B - Appendix D, respectively.

$$\rho(\vec{u} \bullet \nabla)\vec{u} - \mu\nabla^2\vec{u} + \nabla \mathrm{p} = 0, \nabla \bullet \vec{u} = 0 \tag{2}$$

$$k_n = \frac{Q\mu L}{A\Delta P} \tag{3}$$

$$\tau_w = \mu\dot{\gamma}$$

where

$$\dot{\gamma} = \sqrt{2\dot{\varepsilon}_{ij} : \dot{\varepsilon}_{ij}} \tag{4}$$

2.3. Non-Newtonian fluid model

Human blood is a complex heterogeneous mixture, which consists of red blood cells, white blood cells, and platelets combined within the liquid plasma. The physical properties of the blood lie in the interaction of these components with surrounding conditions [40]. In addition, the effective properties of the blood may change based on the viscosity of plasma, hematocrit level, blood cell distribution, mechanical properties of blood cells, and applying forces. To account for the rheology of the blood, several non-Newtonian models have been proposed accordingly. However, despite several rheological models proposed in the literature, Carreau-Yasuda is among the most widely used ones and, thus, chosen in the present work [41].

Thus, the Carreau-Yasuda model is formulated as seen in Eq. (5). According to Eq. (5), μ_0 and μ_∞ are the viscosities at shear rates of zero and infinity, which represent the upper and lower bounds of the blood viscosity, respectively. λ and n are the fitting parameters for the Carreau-Yasuda model. Based on the results from Fedosov et al. [24], Table 1 summarized the viscosity models and fitting parameters which are presently adopted. In addition, Fig. 2 displayed both Newtonian and non-Newtonian fluid viscosities. For the non-Newtonian viscosity, it could be seen that the viscosity exhibits the rate-dependent behavior at the shear rate approximately between 0.01 and 1000 s^{-1}, spanning mostly five orders of magnitude.

$$\mu_c(\dot{\gamma}) = \mu_\infty + (\mu_0 - \mu_\infty)\left(1 + (\lambda\dot{\gamma})^2\right)^{\frac{n-1}{2}} \tag{5}$$

2.4. Surface characterization

Although TPMS structures could be formulated based on the set of implicit equations, it is intriguing to see if the surface characteristics could be correlated with physical responses and manufacturing defects. Experimental studies showed that cells adhered and proliferated non-uniformly based on different curvatures [42,43]. Thus, the importance of Gaussian curvature was emphasized in designing cell tissue scaffolds [43,44]. In addition, Jones et al. showed that geometric deviation of the TPMS structure is highly related to inclination angle and Gaussian curvatures [45]. Greater positional errors were observed with lower inclination angles and less curvy surfaces. As a result, Gaussian curvature and inclination angle of Gyroid samples would be examined in the present work. Fig. 3a - Fig. 3c displayed a schematic of different Gaussian curvatures with positive, negative, and zero values, respectively. Although Gaussian curvature could be determined from the product of two principal curvatures as shown in Eq. (6), Mackay proposed the set of the

Table 1
Newtonian and non-Newtonian blood viscosity models.

Parameters	Units	Models	
		Newtonian	Carreau-Yasuda non-Newtonian model
μ_∞	Pa·s	0.0035	0.0035
μ_0	Pa·s	–	0.25
λ	s	–	69.1
n	–	–	0.3621

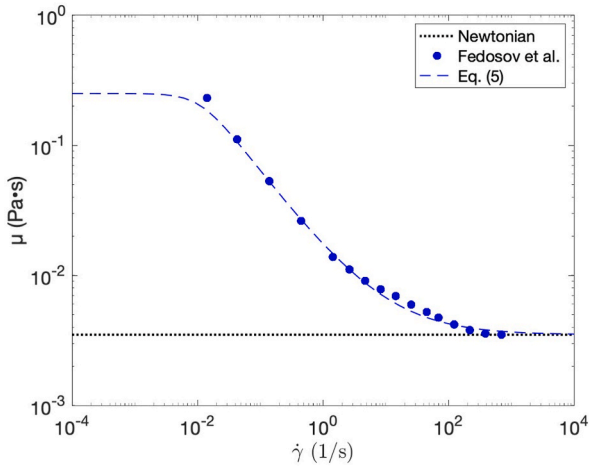

Fig. 2. Newtonian and non-Newtonian viscosity of human blood. Experimental results were obtained from Fedosov et al. [24]. The fitting was based on the Carreau-Yasuda model as shown in Eq. (5).

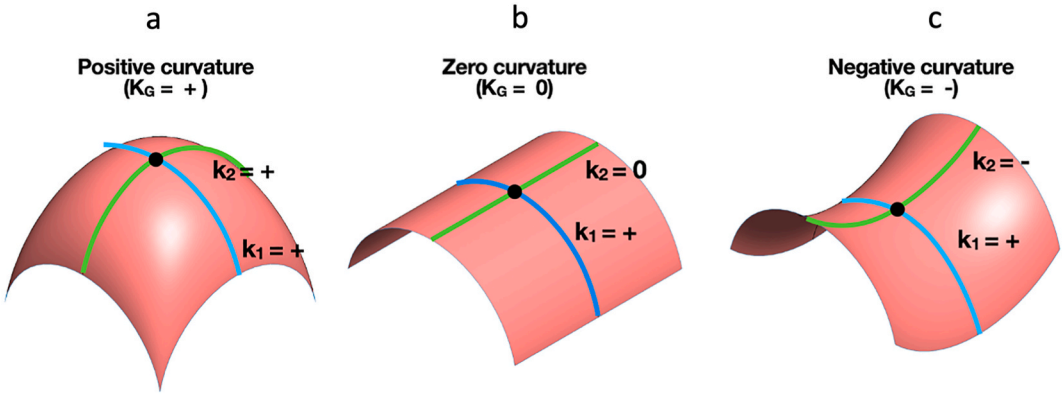

Fig. 3. Illustration of different Gaussian curvatures, showing a) Positive curvature, b) Zero curvature, and c) Negative curvature, respectively.

derivative equations as shown in Eq. (7) to determine analytically local Gaussian curvatures [46]. Consequently, Eq. (7) was adopted and implemented in MATLAB. Besides, the inclination angle was based on the angle of the surface relative to the horizontal plane (XY-plane). According to Fig. 4a, the vector $\hat{k}$ and $\hat{n}$ are the normal vectors of the horizontal and selected planes, respectively. An angle,

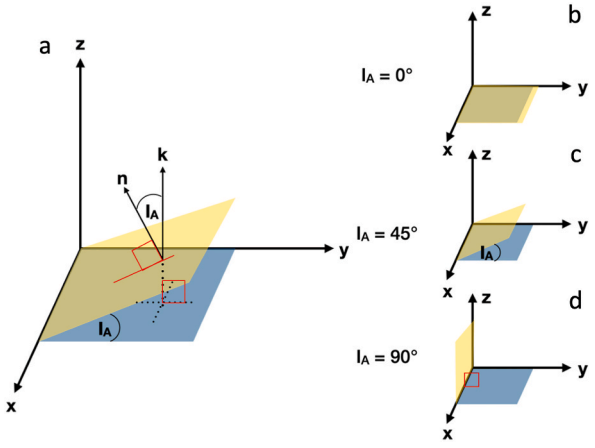

Fig. 4. a) Inclination angle of a plane in 3D system, b) Inclination angle of 0°, c) Inclination angle of 45°, and d) Inclination angle of 90°.

I_A, defines an inclination angle and could be calculated from Eq. (8). Subsequently, Fig. 4b–d show inclination angles of 0°, 45°, and 90°, respectively.

$$K_G = k_1 k_2 \tag{6}$$

$$K_G = \frac{\Delta}{\left(f_x^2 + f_y^2 + f_z^2\right)^2}$$

where

$$\Delta = \begin{vmatrix} f_{xx} & f_{xy} & f_{xz} & f_x \\ f_{yx} & f_{yy} & f_{yz} & f_y \\ f_{zx} & f_{zy} & f_{zz} & f_z \\ f_x & f_y & f_z & 0 \end{vmatrix} \tag{7}$$

$$I_A = cos^{-1}\left(\frac{|\hat{n} \bullet \hat{k}|}{|\hat{n}|\,|\hat{k}|}\right) \tag{8}$$

3. Experiments

3.1. Sample fabrication

Gyroid samples were fabricated using the LPBF system, TRUMPF TruPrint 1000. Ti–6Al–4V was a material of choice due to its biocompatibility and wide adoption in medical applications [13]. The production was carried out under the low oxygen condition, where the Argon was continuously supplied to the build chamber. The process parameters consist of laser power of 90 W, scanning speed of 905 mm/s, hatch spacing of 80 μm, laser diameter of 55 μm, and layer thickness of 20 μm. After the build was completed, samples were removed from the substrate using the wire electrical discharge machining. Besides, samples did not undergo any post-treatment process. Followingly, printed samples were subjected to surface and geometrical characterization using the digital microscope and micro-computed tomography, respectively.

3.2. Geometrical characterization

A non-destructive assessment, micro-CT, was carried out in the as-built state to determine the overall volume and geometrical errors. Fig. 5a - Fig. 5c shows the schematic for the micro-CT, which was performed using the Bruker SkyScan 1173 scanner. The scanning system consists of X-ray source, sample, and X-ray detector. The voxel resolution was set to 20 μm. Based on the micro-CT, the

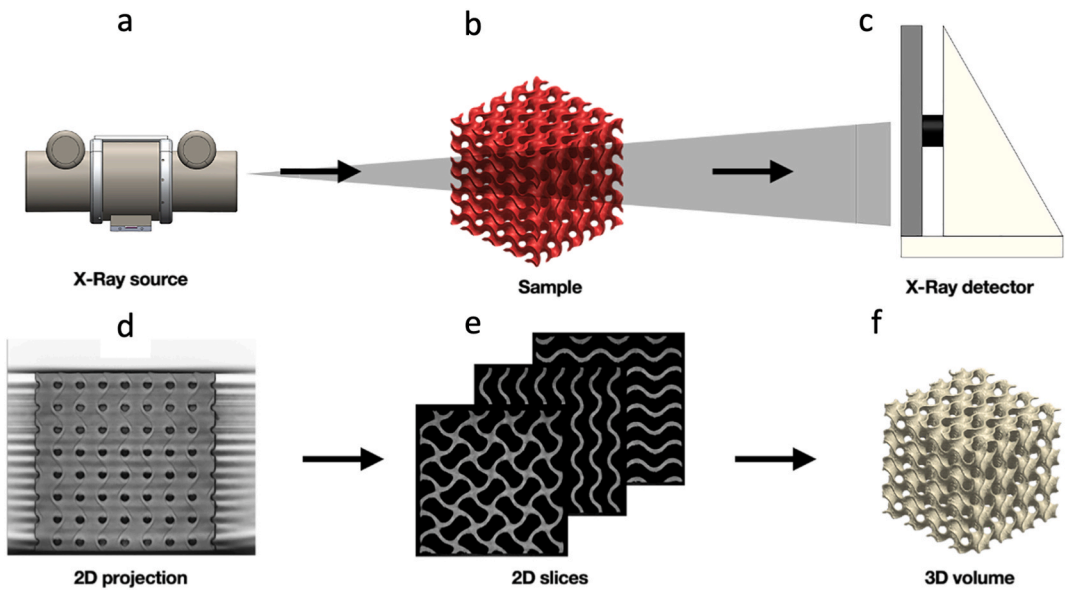

Fig. 5. (Top) Schematic for a micro-computed tomography consisting of a) X-ray source, b) Sample, and c) X-ray detector. (Bottom) Re-construction of 2D CT images into a 3D object consisting of d) 2D projection of the sample, e) 2D slices of the sample, and f) Reconstruction of 2D slices into 3D model.

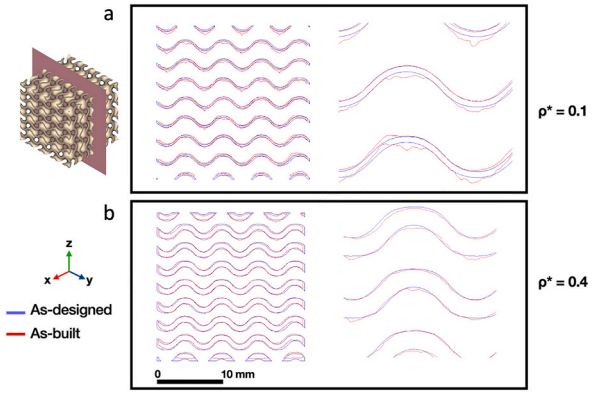

Fig. 6. Determination of domain deviation between CAD and reconstructed models from micro-CT for the samples with a) relative density 0.1 and b) relative density 0.4.

series of 2D images were created along the height. Therefore, to reconstruct 2D images into 3D objects, the Simpleware ScanIP software was utilized as seen in Fig. 5d–f. The reconstructed objects were used to assess experimental samples and generation of as-built CFD domains. Moreover, the comparison between as-designed and as-built profiles was carried out to assess the geometric deviation. To do so, each vertex in the CAD model would find the nearest points in the reconstructed geometry. Then, a geometric error is determined by a minimum Euclidean distance. Fig. 6a and b illustrated the deviated geometry for the sample with relative densities of 0.1 and 0.4, respectively. According to the figures, it could see that the deviated domain can offset both inward and outward from as-designed geometry, referring that the printed parts can be either thicker or thinner than the CAD model. Additionally, even though a deviated profile can be classified as either surface roughness, waviness, or form errors based on the texture wavelength [47], the present work did not attempt to differentiate them and referred to the deviated profiles as geometry deviation. In addition, although micro-CT may reveal surface features from manufacturing, its resolution is insufficient to capture precisely the surface roughness. Thus, to examine the surface roughness, digital microscopy, KEYENCE VHX-series 5000, was utilized. 28 sampling points were taken on each sample, in which the average roughness was determined and reported.

4. Results

4.1. Geometrical deviation of additively manufactured Gyroid structures

An initial inspection showed no apparent cracks for all samples after the build. Therefore, samples were removed from the substrate as shown in Fig. 7a, and the reconstructed models from micro-CT were shown in Fig. 7b. In addition, to explore the surface roughness, Fig. 8a displayed the surface features of the as-built samples. In addition, surface topographies from digital microscopy were shown in Fig. 8b. Fig. 8c displayed surface profiles at higher magnification for roughness assessment. 28 measurements were performed for each sample, in which the arithmetical mean height, S_a, and its standard deviation were 14 ± 2, 19 ± 3, 17 ± 2, and 19 ± 1 μm for the samples with the relative densities of 0.1, 0.2, 0.3, and 0.4, respectively. From these results, it could notice that the average surface roughness does not show a strong dependency on the relative density of samples. Furthermore, after micro-CT reconstruction, Fig. 9a - Fig. 9d illustrated the geometric deviation between as-designed and as-built Gyroid structures for the samples with relative densities from 0.1 to 0.4. According to Fig. 9a–d, it could see that the geometric deviation varied in different regions of the structures. Therefore, geometric deviation may correlate with surface characteristics, where such assessment would be performed in the latter section. Fig. 9a–d also showed that geometric deviation did not strongly vary with height (z-axis) or along the cross-section of the sample (x- and y-axis). Therefore, it may imply that the sample dimension might not be a significant factor affecting a deformation pattern.

Moreover, Fig. 10 exhibited a box plot representation of the as-built deviation. In Fig. 10, the blue box describes the data between the 25th and 75th percentile, and the black lines describe data between the 5th and 95th percentile. In addition, the red line indicates the average value, where the average values were also shown in the figure. The deviation was extracted from approximately 500,000 nodal points for all samples. According to Fig. 10, the geometrical deviation tended toward the negative values, implying that printed samples were smaller than the designed ones. In addition, the average deviation was comparable for the samples with relative densities of 0.1, 0.2, and 0.3. However, the average deviation seemed to be significantly more negative for the sample with the relative density of 0.4. These results were consistent with Sombatmai et al. [17] who observed a tendency of the undersizing in large samples. Additionally, as-designed and as-built volumes were compared as shown in Table 2. According to Table 2, the volume errors increased with greater relative densities. At the relative density of 0.1, the difference between as-designed and as-built models was around 0.001%. However, such a difference increased to 3.4% at a relative density of 0.4. Nevertheless, despite a geometric deviation, the results from micro-CT reconstruction showed that the LPBF process can fabricate complex parts with satisfactory precision.

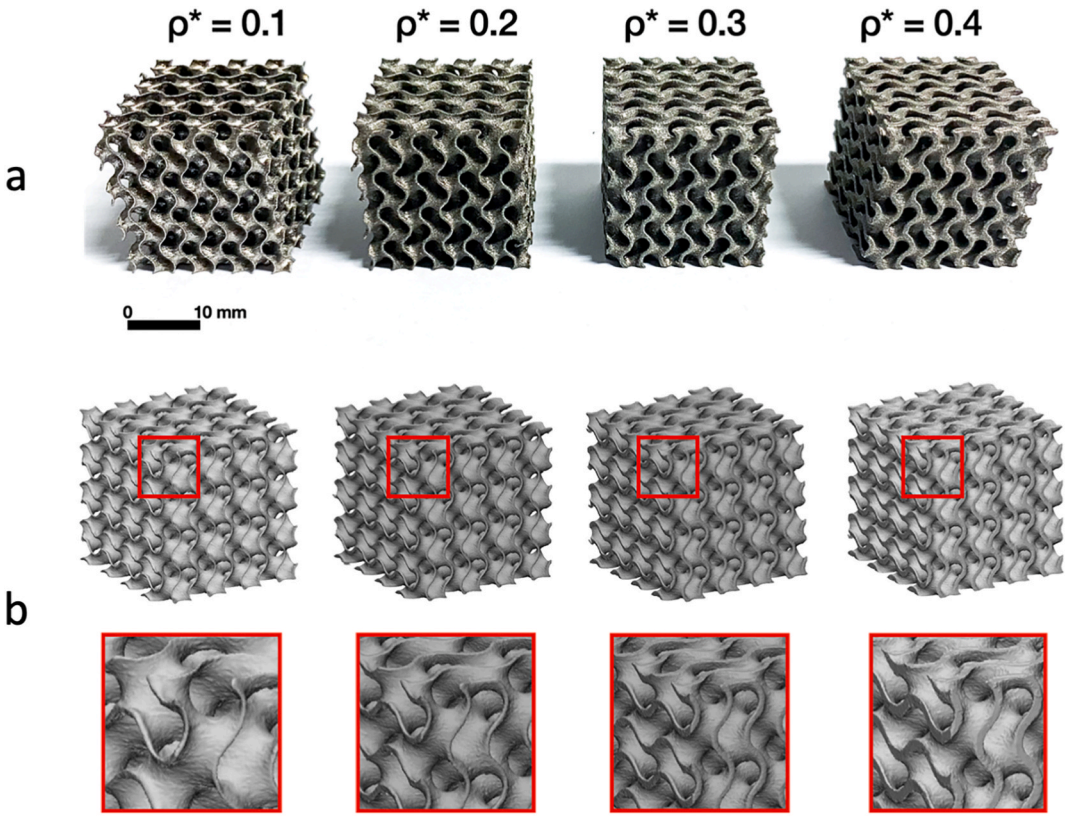

Fig. 7. Additively manufactured Gyroid samples with the relative densities of 0.1, 0.2, 0.3, and 0.4. a) Experimental samples and b) Reconstructed models from micro-CT.

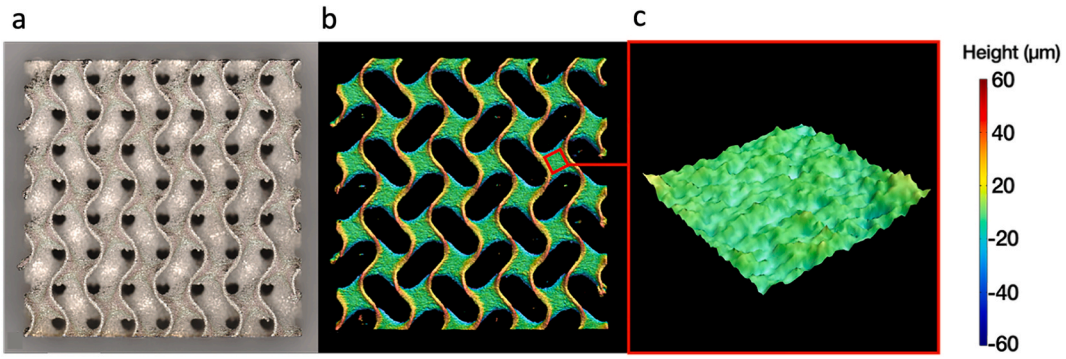

Fig. 8. a) As-built surface of an additively manufactured Gyroid, b) As-built surface profile from digital microscopy, and c) As-built surface profile at high magnification for surface roughness assessment.

4.2. Influence of geometrical defects on flow behavior

In this section, the simulations were performed using only Newtonian viscosity. The aim was to reveal the influence of manufacturing defects on fluid behaviors. Fig. 11a - Fig. 11d illustrated the streamlines, velocity profiles, and fluid-induced wall shear stress contours for as-designed and as-built models for the sample with a relative density of 0.1. According to Fig. 11a and b, the velocity profiles were strongly affected by the geometrical architecture. Although the inlet velocity of 0.5 mm/s was applied, the internal velocity could be as high as 2 mm/s. In addition, non-uniform fluid-induced wall shear stress could be seen in Fig. 11c and d, where the shear stress could vary from as close to zero to as high as 20 mPa. Nonetheless, despite complex velocity and stress contours, Figs. 11a–d illustrated that both as-designed and as-built models provided mostly indistinguishable results. Subsequently, Table 3 and Table 4 reported the average fluid-induced wall shear stress and average pressure drop, respectively, for further comparison.

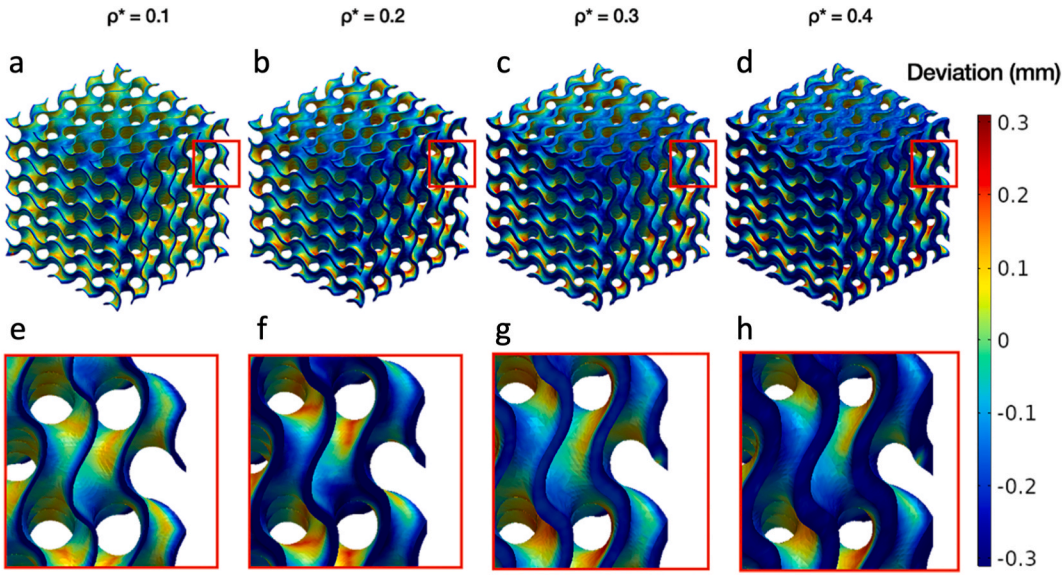

Fig. 9. (a–d) Geometrical deviation contours of as-built Gyroids with relative densities from 0.1 to 0.4, and (e–h) Geometrical deviation contours at high magnification for the sample with relative densities from 0.1 to 0.4.

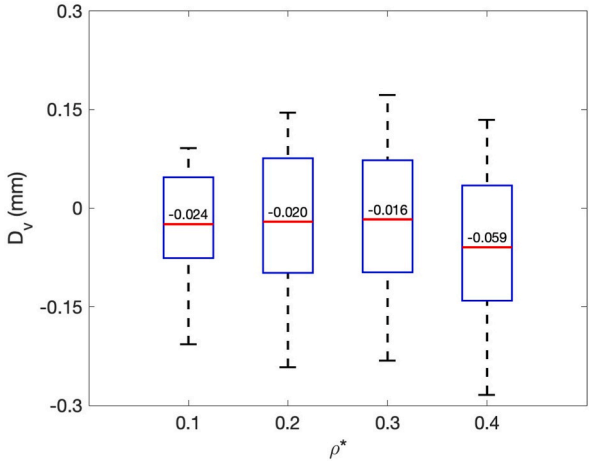

Fig. 10. Box plot representation of geometrical deviation of as-built Gyroid at the relative densities from 0.1 to 0.4.

Table 2
Volume comparison between as-designed and as-built Gyroid models.

As-designed volume (mm^3)	As-built volume (mm^3)	As-designed ρ*	As-built ρ*
800	793.5	0.1	0.099
1600	1555.4	0.2	0.194
2400	2291.4	0.3	0.286
3200	2929.8	0.4	0.366

According to Table 3, the average shear stress deviation became larger with greater relative densities, in which the maximum deviation could be up to 23%. On the other hand, the deviation in the pressure drop was only around 5–7% for all samples. The marginal difference between as-designed and as-built models is somewhat surprising since one would expect that the intrinsic defects from the LPBF process would noticeably alter the physical responses compared to those from the as-designed model. From the macro perspective, the defect from the LPBF process could be from oversizing and undersizing, in which the printed samples could appear either larger or smaller than the CAD model. The surface roughness, on the other hand, could be seen as a defect at the micro level. Typically, both macro and micro defects affect physical behaviors synergistically. Nonetheless, there are three reasons which may

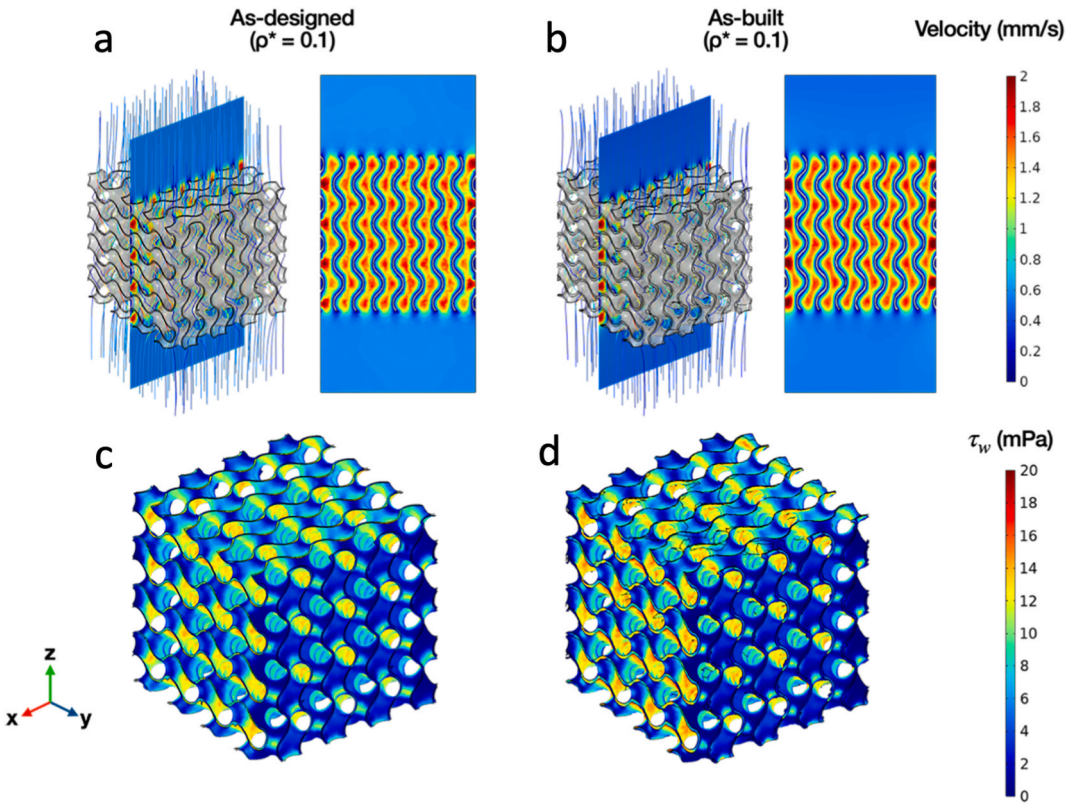

Fig. 11. Comparison of (a, b) velocity profiles and (c, d) wall shear stress contours for as-designed and as-built models at the relative density of 0.1.

Table 3
Average fluid-induced wall shear stress comparison between as-designed and as-built models.

As-designed ρ*	$\tau_{w,\ avg}$ (mPa)		Deviation between as-designed and as-built simulation models
	As-designed	As-built	
0.1	7.5	7.5	0.4%
0.2	8.7	9.2	5.8%
0.3	9.2	10.1	9.9%
0.4	14.2	10.9	−22.9%

Table 4
Pressure drop comparison between as-designed and as-built models.

As-designed ρ*	ΔP (Pa)		Deviation between as-designed and as-built simulation models
	As-designed	As-built	
0.1	0.48	0.51	6.3%
0.2	0.78	0.73	−6.4%
0.3	1.02	0.95	−6.9%
0.4	1.64	1.72	4.9%

explain the minor deviation between the CAD and defects-embedded models. Firstly, the quality of surface reconstruction depended greatly on a CT voxel resolution. Due to the scan of the entire sample, the voxel size was chosen to be 20 μm. Since the average surface roughness shown in the previous section was around 15–20 μm, the 20 μm voxel size may not be sufficient to capture precisely the surface profiles. Secondly, according to the parameters adopted in the present work, the Reynolds number based on the channel size would be around 1. With such a low Reynolds number, the effect of surface roughness on local flow fields may be mostly inconsequential. Lastly, based on the volume comparison shown in Table 2, the deviations between as-designed and as-built volumes were between 1 and 8%. The maximum volume deviation was seen at the relative density of 0.4. However, a subtle macro defect may have a minute impact on flow behaviors. Of note, although we noticed the negligible effect of manufacturing defects on flow responses, the

severity of the defects could change based on geometries, sample sizes, materials, and LPBF process conditions. Therefore, the finding presented herein may only apply to the selected geometry, material, and manufacturing system.

4.3. Influence of non-Newtonian model on flow behavior

As mentioned previously, fluid-induced wall shear stress can act as a stimulus for bone tissues [48]. Although suitable wall shear stress may promote bone tissue proliferation, insufficient or excessive shear stress may lead to inactive cell responses and cell damage, respectively [7]. In this regard, a high-fidelity CFD model can provide useful information for the design of bone substituting architecture. Although the manufacturing defects including geometric deviation and surface roughness were shown to exhibit slight effect of fluid responses, blood viscosity is another important factor, dictating local flow characteristics. The present work captured the effect of shear rate on blood viscosity using the Carreau-Yasuda model as seen in Eq. (5). As a result, this section provided an assessment on the effect of non-Newtonian properties on flow responses. Both Newtonian and non-Newtonian viscosity models were utilized with the as-designed models. The same boundary conditions were applied for both viscosities.

Fig. 12a–d displayed flow fields and wall shear stress contours for both Newtonian and non-Newtonian models. Fig. 12a and b showed the velocity profiles under Newtonian and non-Newtonian properties, respectively. According to the figures, the velocity profiles of both viscosities were largely indistinguishable, where the maximum flow velocity was around 2 mm/s. However, the stress contours in Fig. 12c and d clearly illustrated the greater shear stress for the non-Newtonian model. Although higher shear stress can be anticipated with higher fluid viscosity, it is critical to determine the deviation's magnitude from the Newtonian model. Thus, Fig. 13a - Fig. 13d compared the shear stress distribution for both Newtonian and non-Newtonian viscosities for the samples with relative densities from 0.1 to 0.4. In addition, the range of favorable shear stresses, which were found to support the growth of bone tissue, was also defined in the figures. According to Karuna et al. [7], the favorable shear stresses were between 0.05 and 10 mPa. According to Fig. 13a–d, the distribution for both viscosity models was similar, in which the left-skewed pattern was observed. However, with a non-Newtonian property, the shear stress distribution shifted toward the higher value region. Table 5 displayed the average shear stresses for both Newtonian and non-Newtonian models, in which those of non-Newtonian were a factor of 1.5–2 greater than those of Newtonian ones. A maximum deviation occurred at the low relative density and was reduced when the relative density increased. Moreover, it was observed that the average shear stress was more sensitive to the sample's relative density under the Newtonian model. With the Newtonian model, the average shear stress increased by mostly a factor of two when the relative density changed from 0.1 to 0.4. However, such an increase is seen to be only 40% when the non-Newtonian model was applied. Furthermore, Table 6 indicated the resulting shear stress, which falls within the favorable stress regime for bone tissue ingrowth. For the Newtonian results, the matching

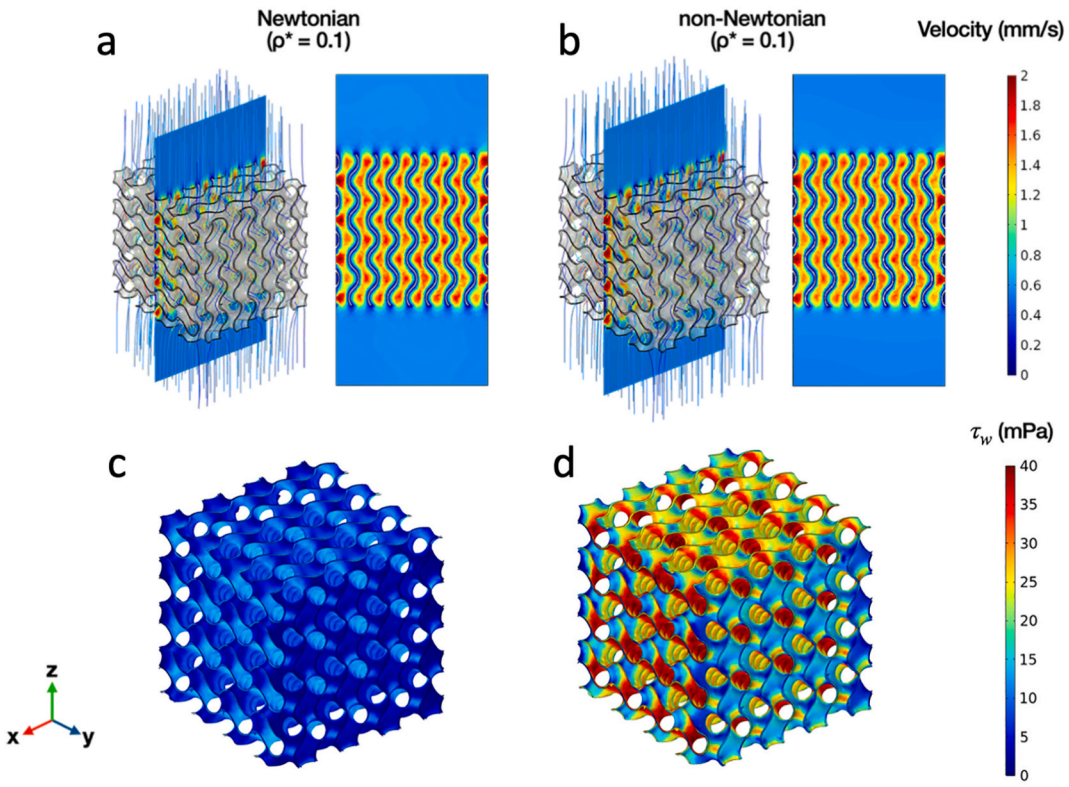

Fig. 12. Comparison of (a, b) velocity profiles and (c, d) wall shear stress contours for the models with Newtonian and non-Newtonian viscosities.

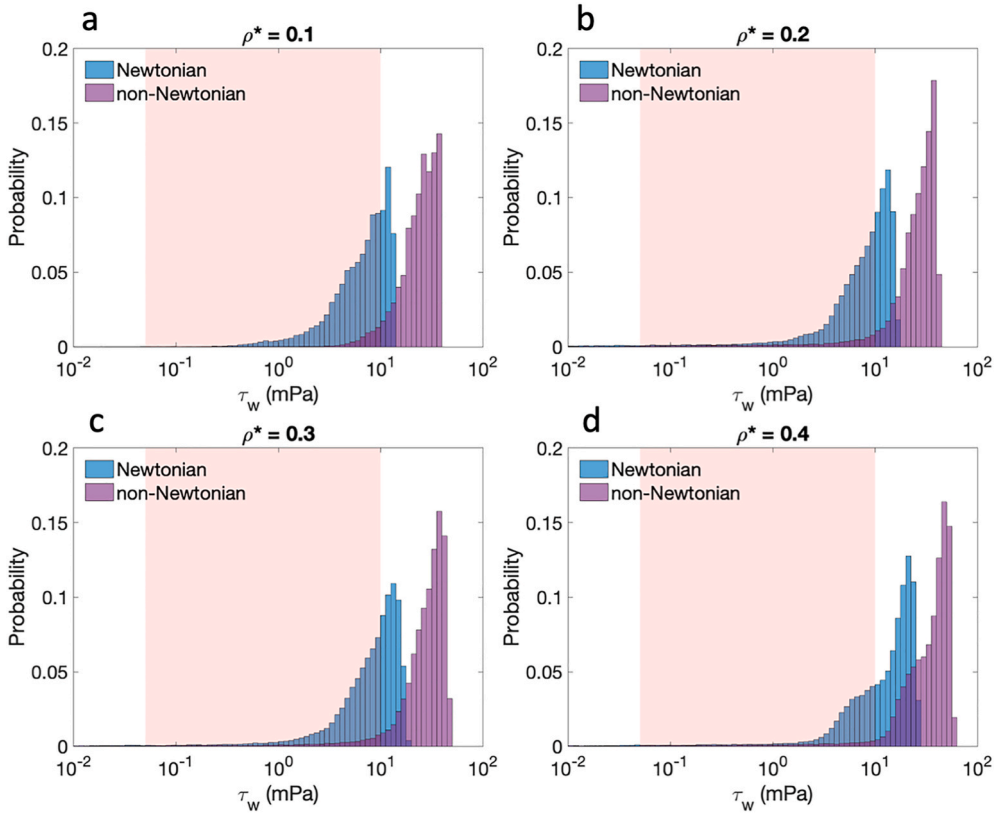

Fig. 13. Wall shear stress distribution under Newtonian and non-Newtonian properties for the samples with the relative density of a) 0.1, b) 0.2, c) 0.3, and d) 0.4. A shaded area defined the favorable wall shear stress for the growth of bone tissue [7].

Table 5
Average fluid-induced wall shear stress comparison between Newtonian and non-Newtonian viscosity models.

As-designed ρ*	$\tau_{w,\ avg}$ (mPa)		Deviation between Newtonian and non-Newtonian viscosity models
	Newtonian	non-Newtonian	
0.1	7.5	25.2	236%
0.2	8.7	26.6	206%
0.3	9.2	29.1	216%
0.4	14.2	35.5	150%

Table 6
Resulting fluid-induced wall shear stress that falls within the favorable regime for bone growth.

As-designed ρ*	Newtonian model	non-Newtonian model
0.1	70.5%	5.3%
0.2	54.9%	7.4%
0.3	52.6%	6.0%
0.4	31.6%	4.6%

shear stress could be as high as 70% for the sample with relative density of 0.1 and reduced to 31.6% when the relative density increased to 0.4. On the contrary, since the shear stress became much higher with the non-Newtonian model. The shear stress falling into the favorable regime was only around 5%. Although the resulting shear stress can be modified with the change in unit cell sizes, these results emphasized the importance of constitutive models for blood responses. An overly simplified blood viscosity may lead to a sub-optimal scaffold design, especially when the fluid-induced wall shear stress is of great concern. In addition, although Table 5 and Fig. 13 displayed the considerable impact of non-Newtonian viscosity on shear stress responses, the range of shear rates encountered by the fluid within the scaffolds was not evident. Therefore, Fig. 14 displayed the shear rate distribution for the scaffolds with relative densities of 0.1 and 0.4. According to Fig. 14, resulting shear rates for both specimens were within the comparable ranges of 10^{-1} and

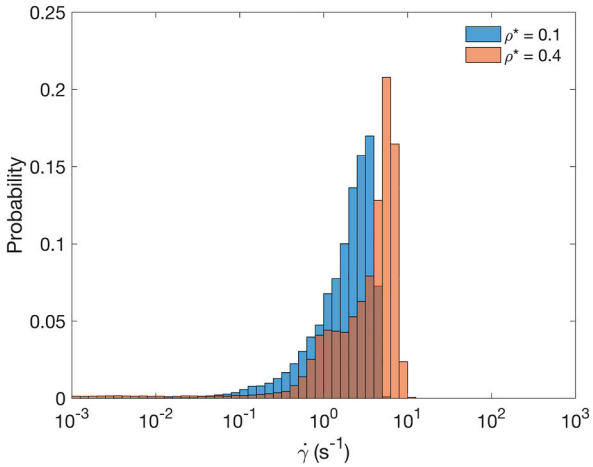

Fig. 14. Comparison of shear rate distribution between samples with the relative density of 0.1 and 0.4.

10^1 s^{-1}. These shear rate ranges were in accordance with the upper and lower limits of the blood viscosity model, which were between 10^{-2} and 10^3 s^{-1}. Thus, the CFD analysis indicated clearly that resulting shear rates from the flow within the Gyroids are under the ranges, where non-Newtonian effect is critically important.

Moreover, the pressure drops, which could indicate nutrient transportability through the structure, were shown and compared for both viscosity models as seen in Fig. 15. According to Fig. 15, the influence of the non-Newtonian model for both average wall shear stress and pressure drop was noticeably similar. The responses from the non-Newtonian model were higher than those from the Newtonian model by the factors of 1.5 and 2. The greatest difference was seen in the least dense sample, and the difference between both viscosity models became more subtle at higher relative densities.

4.4. *Correlations between geometrical features and physical responses*

Previous sections examined the manufacturing defects and fluid behaviors of Gyroid TPMS scaffolds. Nonetheless, a better understanding of the influence of geometrical features would allow us to quickly assess the parameters that dictate outputs such as part deviation and fluid-induced shear stress. Followingly, Fig. 16a and b displayed 3D contours of Gaussian curvatures and inclination angles, respectively. In addition to 3D contours, the distribution of Gaussian curvatures and inclination angles was subsequently shown in Fig. 16c and d. According to Fig. 16c, the curvature deviation was seen mostly between -1.2 and 0 mm^{-2}. In addition, the inclination angle exhibited a wide distribution from 0° to 90° as seen from Fig. 16d. At 90°, the surface angle would be parallel with the incoming flow while the incoming flow would be perpendicular to the surface at 0° surface angle. Fig. 17 showed the normalized heat map combining Gaussian curvature and inclination angle. A similar heat map has been reported previously by Jones et al. [45]. By comparing Fig. 17 with the results from Jones et al., we noticed that although the curvature and inclination angle heat map looks

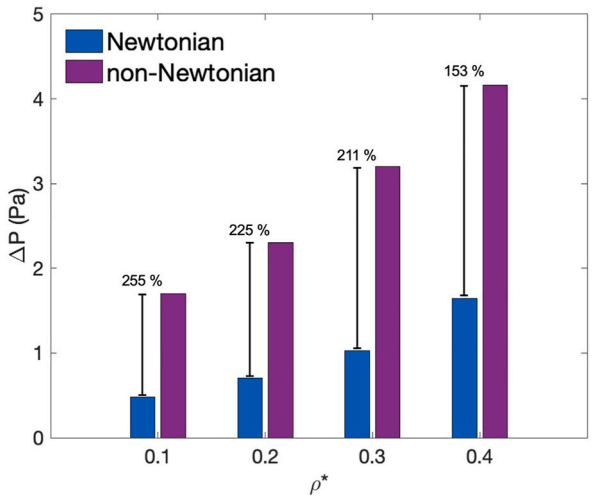

Fig. 15. Pressure drop comparison between Newtonian and non-Newtonian models for the samples with the relative density from 0.1 to 0.4.

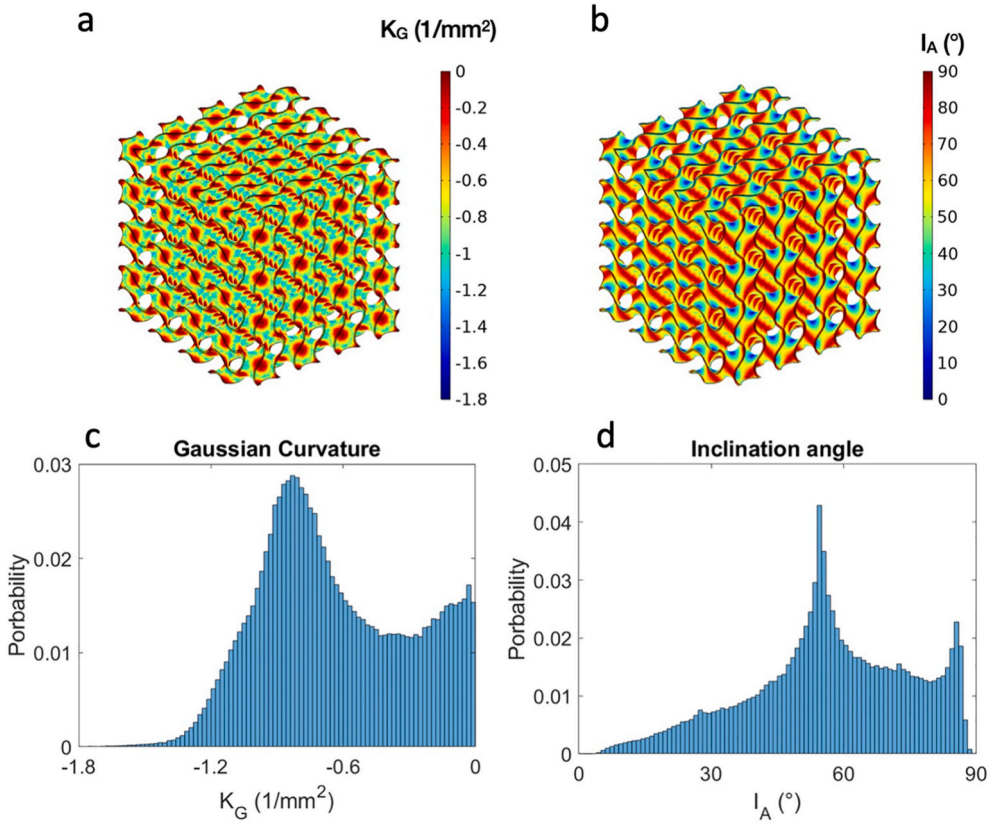

Fig. 16. a) Contour of Gaussian curvature, b) Contour of inclination angle, c) Normalized distribution of Gaussian curvature, and d) Normalized distribution of inclination angle. Results were plotted for the Gyroid with a relative density of 0.1.

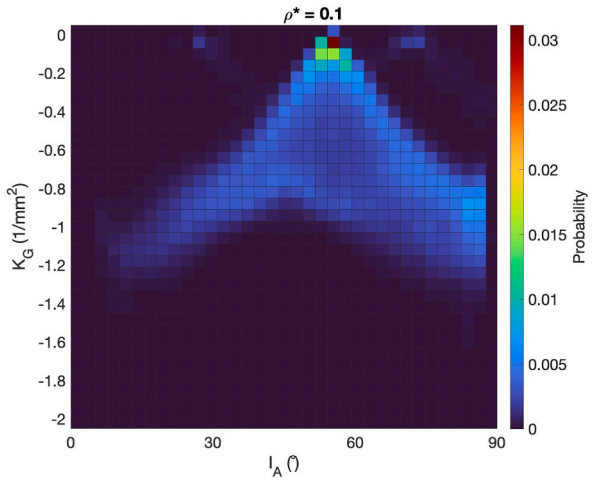

Fig. 17. Normalized heat map for Gaussian curvature and inclination angle for Gyroid with relative density of 0.1.

relatively similar, the magnitude of the curvature was greatly different. Our maximum curvature was noticeably larger than that of Jones et al. [45]. Nonetheless, the difference in the curvature was comprehensible since Jones et al. adopted the unit cell size of 10 mm while that of 5 mm was used in the present work. A smaller unit cell size can lead to a larger curvature. On the other hand, the inclination angle of the Gyroid is independent of the unit cell size.

According to Jones et al. [45], curvature was noted for its great influence on geometrical accuracy and manufacturability of LPBF samples. Thus, the surface deviation was plotted against curvature as shown in Fig. 18a - Fig. 18d for samples with the relative density

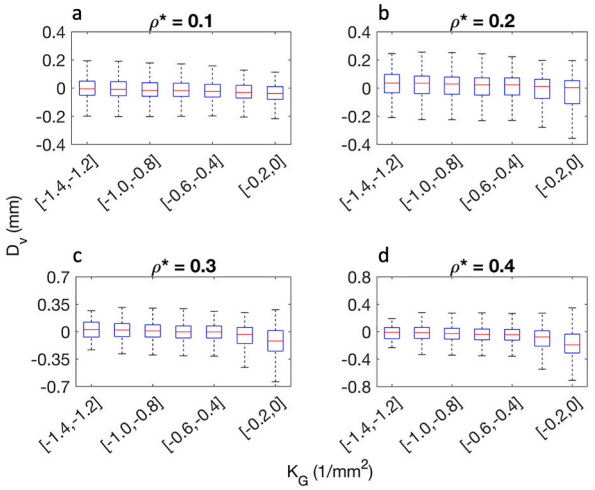

Fig. 18. Comparison between Gaussian curvature and surface deviation for the samples with the relative density of a) 0.1, b) 0.2, c) 0.3, and d) 0.4.

between 0.1 and 0.4. According to the figures, although the effect of curvature on geometry deviation was noticed, such an effect was seen depending on the relative density of the sample. For example, as seen in Fig. 18a, at the relative density of 0.1, the curvature effect on surface deviation seemed highly inconsequential. The geometric deviation varied approximately between −0.2 and 0.2 mm regardless of the surface curvature. On the contrary, the influence of curvature was more apparent at higher relative density. As seen in Fig. 18d, at the relative density of 0.4, the sample deviated greatly when the curvature was close to zero, and the deviation reduced significantly at greater Gaussian curvature. Additionally, it was observed from Table 2 and Fig. 10 that the deviations of relative densities and positional errors were smaller when the samples had lower relative densities. Based on these results, the LPBF process appeared to exhibit better manufacturability for the Gyroid with low density.

In addition to the surface deviation, we assessed the correlation between curvature and inclination angle with resulting shear stress. Of the two variables, we found that the resulting shear stress strongly correlated with the inclination angle. Therefore, the relationship between inclination angle and shear stress was shown in Fig. 19a - Fig. 19d for samples with the relative density between 0.1 and 0.4. And the correlation between curvature and shear stress was shown in Appendix A. According to Fig. 19a–d, the fluid-induced wall shear stress increased with the inclination angle. However, we noted a steep increase at the inclination angle between 0° and 50°. Subsequently, at the inclination angle between 50° and 90°, the magnitude and distribution of shear stress are seemingly identical. In addition, although the inclination angle and fluid-induced shear stress correlated similarly for all samples, the correlation became more signified at higher relative density. For example, as seen in Fig. 19a, at the relative density of 0.1, the average shear stress for the angle between 0° and 10° was 3.5 mPa and became 7.5 mPa under the angle between 80° and 90°. Nonetheless, those average stresses were changed to 4.65 and 20.3 mPa under the same angle intervals for the sample with relative density of 0.4 as seen in Fig. 19d.

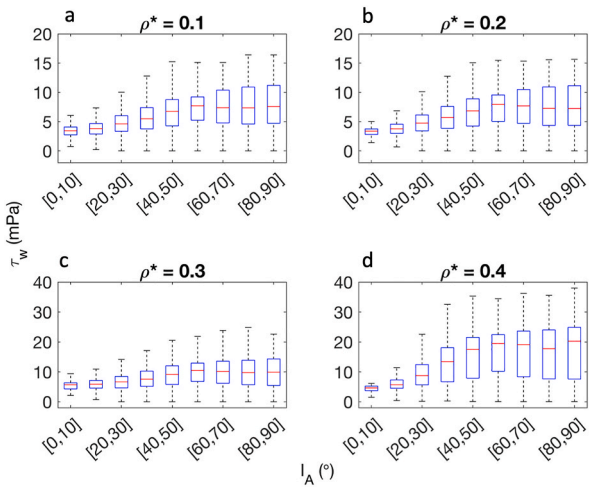

Fig. 19. Comparison between fluid-induced wall shear stress and inclination angle for the samples with the relative density of a) 0.1, b) 0.2, c) 0.3, and d) 0.4.

5. Conclusion

The present study explored the sensitivity of manufacturing defects and fluid viscosity model on the flow behavior of Gyroid TPMS scaffolds. Gyroids with relative densities between 0.1 and 0.4 were made additively using the LPBF process. Digital microscopy was used to measure the surface roughness, and micro-CT was utilized to obtain the reconstructed 3D models. Positional errors were determined by comparing as-built and as-designed models. Subsequently, CFD simulations were carried out to evaluate the effect of the geometrical defects and the non-Newtonian fluid model on pressure drop and fluid-induced wall shear stress. Lastly, an attempt to correlate geometrical characteristics such as Gaussian curvature and inclination angle with surface deviation and local shear stress was made. The conclusion from the present work could be identified as follows.

1. The surface roughness of printed Gyroids was between 14 and 19 μm. In addition, although the surface roughness was not strongly correlated with relative density, we found that the deviation between as-designed and as-built volumes became greater with the increase in the relative density. The volume deviation increased approximately from 1 to 8% when the targeted relative density changed from 0.1 to 0.4. Moreover, the samples explored in the present work exhibited an undersized characteristic compared to the as-designed volume.
2. The pressure drop and fluid-induced shear stress were largely comparable between as-designed and as-built models. The maximum deviation for the average shear stress and pressure drop was approximately 20 and 7%, respectively. It was anticipated that low incoming Reynolds number and limited voxel resolution from micro-CT are a primary reason for a subtle difference between both models.
3. On the other hand, the non-Newtonian viscosity was found to have a significant impact on flow responses. Both average shear stress and pressure drop from non-Newtonian model could be a factor of two greater than those from the Newtonian model. The resulting shear rate from CFD simulation was between 10^{-1} and 10^{1} s^{-1}, which was within the non-Newtonian shear rate regime, which is around 10^{-2} and 10^{3} s^{-1}.
4. We compared the resulting shear stress with favorable stress for tissue growth. Based on Newtonian results, 30–70% of resulting stress falls within the favorable regime. However, those numbers were reduced to approximately 5% when the non-Newtonian model was adopted. This comparison signified the importance of the viscosity model, especially when the resulting shear stress is an output of interest.
5. A better manufacturability was seen for a curvier region. The surface deviation was reduced with larger Gaussian curvature. In addition, the fluid-induced wall shear stress increased with a greater inclination angle, where the steep escalation in the shear stress was seen between the surface angle of 0° and 50°. In addition, the correlation between geometrical features and physical outputs was more noticeable for the samples with greater relative densities.

Author contribution statement

Saran Seehanam: Performed the experiments; Contributed reagents, materials, analysis tools or data; Wrote the paper.
Wares Chanchareon: Contributed reagents, materials, analysis tools or data; Wrote the paper.
Patcharapit Promoppatum: Conceived and designed the experiments; Analyzed and interpreted the data; Contributed reagents, materials, analysis tools or data; Wrote the paper.

Data availability statement

Data will be made available on request.

Declaration of competing interest

The authors declare that they have no known competing financial interests or personal relationships that could have appeared to influence the work reported in this paper.

Acknowledgments

PP would like to acknowledge the financial support from National Research Council of Thailand (NRCT) under the projects with the grant numbers N23D650026 and N42A660524. SS is grateful to the support from National Research Council of Thailand (NRCT) under the project “Influence of geometrical features on flow behavior of TPMS bone scaffolds”.

Appendix A. Correlation between fluid-induced wall shear stress and Gaussian curvature

Fig. 1A illustrated the correlation between fluid-induced wall shear stress and Gaussian curvature for samples with relative densities from 0.1 to 0.4. From the figure, it could see that the fluid-induced shear stress is not strongly correlated with the Gaussian curvature, especially when considering the correlation between fluid-induced wall shear stress and inclination angle as seen in Fig. 19.

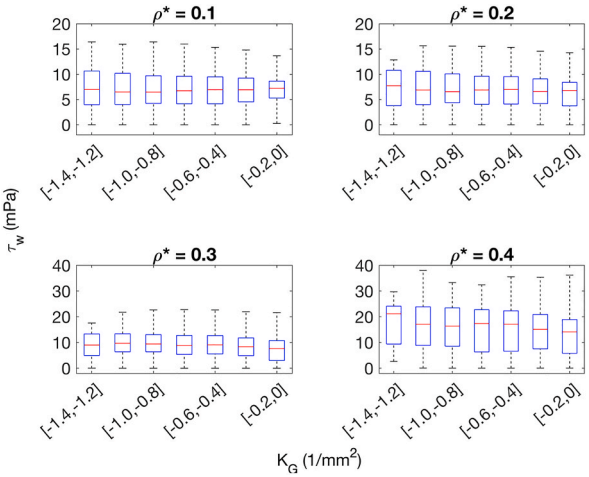

Fig. 1A. Comparison between fluid-induced wall shear stress and Gaussian curvature for samples with relative densities from 0.1 to 0.4

Appendix B. Domain size sensitivity

The domain size sensitivity was determined to ensure that the physical outputs were independent of the cell configuration. In the present work, we changed the configuration of the computational domain from 1 × 1 x 1 to 4 × 4 x 4 as seen in Fig. 2A. Fluid permeability and wall shear stress were determined accordingly as shown in Table 1A. According to Table 1A, resulting fluid responses changed significantly when the domain configuration changed from 1 × 1 x 1 to 2 × 2 x 2. Nonetheless, fluid responses became much more consistent when a domain configuration larger than 2 × 2 x 2 was chosen. As a result, the domain configuration of 4 × 4 x 4 was adopted in the present work.

Table 1A
Domain size sensitivity of permeability and fluid-induced wall shear stress under Newtonian viscosity

Domain configuration	k_n (10^{-9} m^2)	$\tau_{w,avg}$ (mPa)
1 × 1 x 1	14.1	13.97
2 × 2 x 2	21.0	14.01
3 × 3 x 3	21.1	14.24
4 × 4 x 4	21.2	14.20

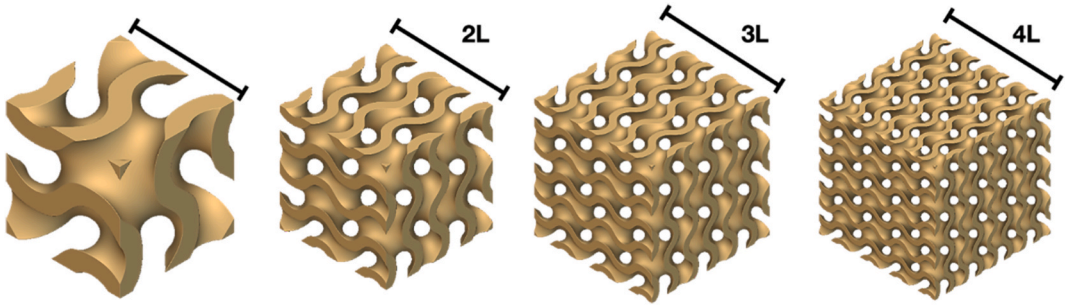

Fig. 2A. Gyroid with a relative density of 0.4 and domain configuration varied from 1 × 1 x 1 to 4 × 4 x 4

Appendix C. : Mesh sensitivity analysis

For mesh sensitivity analysis, the sample with 4 × 4 x 4 configuration was tested with the mesh size varied between 0.2 and 0.5 mm as seen in Fig. 3A. Under the same boundary conditions, the pressure drop and fluid-induced wall shear stress of different mesh sizes were determined and compared as shown in Table 2A. According to Table 2A, the fluid responses changed noticeably when the mesh sizes changed from 0.5 to 0.3 mm. However, when the mesh size changed from 0.3 to 0.2 mm, the pressure drop and fluid-induced shear stress only altered by less than 1%. Therefore, the mesh size of 0.3 mm was adopted in our study.

Table 2A
Mesh sensitivity analysis for CFD simulation

Mesh size (mm)	Number of elements	ΔP (Pa)	$\tau_{w,\ avg}$ (mPa)
0.5	980,329	4.45	34.2
0.4	1,601,111	4.32	35.3
0.3	3,569,410	4.21	35.5
0.2	12,241,678	4.19	35.7

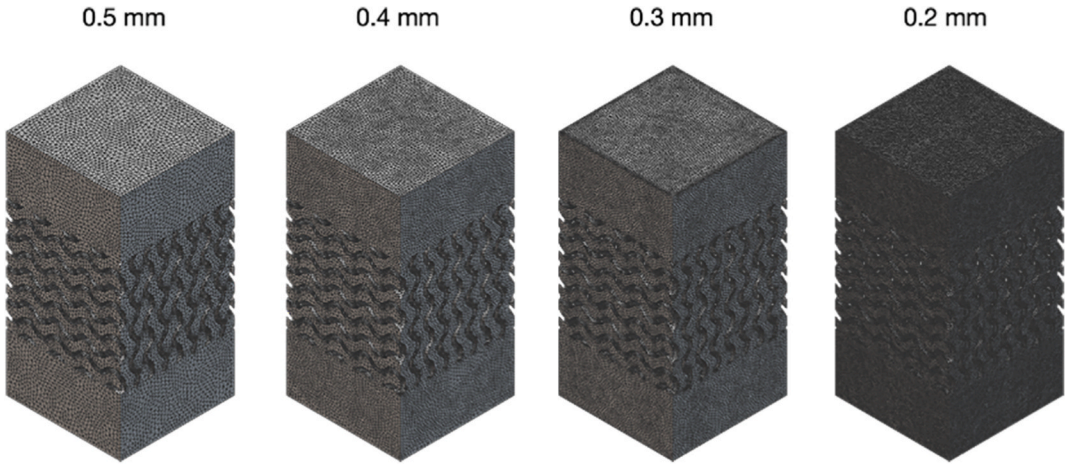

Fig. 3A. Fluid domain with 4 × 4 x 4 configuration, and mesh size varied between 0.2 and 0.5 mm

Appendix D. Numerical model validation. For CFD simulation, the model was validated by comparing present results with those reported by Asbai-Ghoudan et al. [49]. Asbai-Ghoudan et al. studied numerically the fluid permeability of several TPMS scaffolds. In their simulation, a cell configuration of four rows was used, and the Newtonian fluid property was assumed. We compared their results with our prediction as shown in Table 3A. According to Table 3A, results from both studies are in good agreement with a difference of less than 10%. As a result, it could imply that a numerical model adopted in the present work could provide a reasonable prediction of flow responses.

Table 3A
Predicted fluid permeability from Asbai-Ghoudan et al. [49] and present study

ρ*	k_n (10^{-9} m^2)		Difference
	Present study	Asbai-Ghoudan et al.	
0.1	72.9	74.2	1.8%
0.2	44.8	48.3	7.6%
0.3	34.3	35.8	4.3%
0.4	21.1	23.3	9.2%

References

[1] W.E. Frazier, Metal additive manufacturing: a review, J. Mater. Eng. Perform. 23 (2014) 1917–1928.
[2] P. Promoppatum, R. Srinivasan, S.S. Quek, S. Msolli, S. Shukla, N.S. Johan, et al., Quantification and prediction of lack-of-fusion porosity in the high porosity regime during laser powder bed fusion of Ti-6Al-4V, J. Mater. Process. Technol. (2021), 117426, https://doi.org/10.1016/j.jmatprotec.2021.117426.
[3] V.V. Popov, G. Muller-Kamskii, A. Kovalevsky, G. Dzhenzhera, E. Strokin, A. Kolomiets, et al., Design and 3D-printing of titanium bone implants: brief review of approach and clinical cases, Biomed. Eng. Lett. 8 (2018) 337–344, https://doi.org/10.1007/s13534-018-0080-5.
[4] A. Koptioug, L.E. Rännar, M. Bäckström, M. Cronskär, Additive manufacturing for medical and biomedical applications: advances and challenges, Mater. Sci. Forum 783–786 (2014) 1286–1291. https://dx.doi.org/10.4028/www.scientific.net/MSF.783-786.1286.
[5] X. Wang, S. Xu, S. Zhou, W. Xu, M. Leary, P. Choong, et al., Topological design and additive manufacturing of porous metals for bone scaffolds and orthopaedic implants: a review, Biomaterials 83 (2016) 127–141, https://doi.org/10.1016/j.biomaterials.2016.01.012.
[6] M. Cronskär, L.-E. Rännar, M. Bäckström, K.G. Nilsson, B. Samuelsson, Patient-Specific clavicle reconstruction using digital design and additive manufacturing, J. Mech. Des. 137 (2015), 111418, https://doi.org/10.1115/1.4030992.
[7] C. Karuna, T. Poltue, S. Khrueaduangkham, P. Promoppatum, Mechanical and fluid characteristics of triply periodic minimal surface bone scaffolds under various functionally graded strategies, J. Comput. Des. Eng. 9 (2022) 1258–1278.

[8] I. Maskery, N.T. Aboulkhair, A.O. Aremu, C.J. Tuck, I.A. Ashcroft, Compressive failure modes and energy absorption in additively manufactured double gyroid lattices, Addit. Manuf. 16 (2017) 24–29, https://doi.org/10.1016/j.addma.2017.04.003.

[9] D. Ali, M. Ozalp, S.B. Blanquer, S. Onel, Permeability and fluid flow-induced wall shear stress in bone scaffolds with TPMS and lattice architectures: a CFD analysis, Eur. J. Mech-BFluids 79 (2020) 376–385, https://doi.org/10.1016/j.euromechflu.2019.09.015.

[10] S. Ma, Q. Tang, X. Han, Q. Feng, J. Song, R. Setchi, et al., Manufacturability, mechanical properties, mass-transport properties and biocompatibility of triply periodic minimal surface (TPMS) porous scaffolds fabricated by selective laser melting, Mater. Des. 195 (2020), 109034, https://doi.org/10.1016/j.matdes.2020.109034.

[11] S. Zou, Y. Mu, B. Pan, G. Li, L. Shao, J. Du, et al., Mechanical and biological properties of enhanced porous scaffolds based on triply periodic minimal surfaces, Mater. Des. (2022), 110803.

[12] J. Shi, L. Zhu, L. Li, Z. Li, J. Yang, X. Wang, A TPMS-based method for modeling porous scaffolds for bionic bone tissue engineering, Sci. Rep. 8 (2018) 1–10.

[13] L. Li, J. Shi, K. Zhang, L. Yang, F. Yu, L. Zhu, et al., Early osteointegration evaluation of porous Ti6Al4V scaffolds designed based on triply periodic minimal surface models, J. Orthop. Transl. 19 (2019) 94–105.

[14] T. Poltue, C. Karuna, S. Khrueaduangkham, S. Seehanam, P. Promoppatum, Design exploration of 3D-printed triply periodic minimal surface scaffolds for bone implants, Int. J. Mech. Sci. 211 (2021), 106762, https://doi.org/10.1016/j.ijmecsci.2021.106762.

[15] S.H. Cartmell, B.D. Porter, A.J. García, R.E. Guldberg, Effects of medium perfusion rate on cell-seeded three-dimensional bone constructs in vitro, Tissue Eng. 9 (2003) 1197–1203.

[16] H. Masuo, Y. Tanaka, S. Morokoshi, H. Yagura, T. Uchida, Y. Yamamoto, et al., Influence of defects, surface roughness and HIP on the fatigue strength of Ti-6Al-4V manufactured by additive manufacturing, Int. J. Fatig. 117 (2018) 163–179.

[17] A. Sombatmai, V. Uthaisangsuk, S. Wongwises, P. Promoppatum, Multiscale investigation of the influence of geometrical imperfections, porosity, and size-dependent features on mechanical behavior of additively manufactured Ti-6Al-4V lattice struts, Mater. Des. 209 (2021), 109985, https://doi.org/10.1016/j.matdes.2021.109985.

[18] A. Du Plessis, I. Yadroitsev, I. Yadroitsava, S.G. Le Roux, X-ray microcomputed tomography in additive manufacturing: a review of the current technology and applications, 3D Print. Addit. Manuf. 5 (2018) 227–247.

[19] S. Lee, B. Rasoolian, D.F. Silva, J.W. Pegues, N. Shamsaei, Surface roughness parameter and modeling for fatigue behavior of additive manufactured parts: a non-destructive data-driven approach, Addit. Manuf. 46 (2021), 102094.

[20] B. Lozanovski, M. Leary, P. Tran, D. Shidid, M. Qian, P. Choong, et al., Computational modelling of strut defects in SLM manufactured lattice structures, Mater. Des. 171 (2019), 107671.

[21] T. Pires, J. Santos, R.B. Ruben, B.P. Gouveia, A.P. Castro, P.R. Fernandes, Numerical-experimental analysis of the permeability-porosity relationship in triply periodic minimal surfaces scaffolds, J. Biomech. 117 (2021), 110263, https://doi.org/10.1016/j.jbiomech.2021.110263.

[22] H. Montazerian, E. Davoodi, M. Asadi-Eydivand, J. Kadkhodapour, M. Solati-Hashjin, Porous scaffold internal architecture design based on minimal surfaces: a compromise between permeability and elastic properties, Mater. Des. 126 (2017) 98–114.

[23] H.A. Baieth, Physical parameters of blood as a non-Newtonian fluid, Int. J. Biomed. Sci. IJBS 4 (2008) 323.

[24] D.A. Fedosov, W. Pan, B. Caswell, G. Gompper, G.E. Karniadakis, Predicting human blood viscosity in silico, Proc. Natl. Acad. Sci. USA 108 (2011) 11772–11777, https://doi.org/10.1073/pnas.1101210108.

[25] Y. Jiang, J. Zhang, W. Zhao, Effects of the inlet conditions and blood models on accurate prediction of hemodynamics in the stented coronary arteries, AIP Adv. 5 (2015), 057109, https://doi.org/10.1063/1.4919937.

[26] P. Reymond, F. Perren, F. Lazeyras, N. Stergiopulos, Patient-specific mean pressure drop in the systemic arterial tree, a comparison between 1-D and 3-D models, J. Biomech. 45 (2012) 2499–2505, https://doi.org/10.1016/j.jbiomech.2012.07.020.

[27] A.D. Caballero, S. Laín, Numerical simulation of non-Newtonian blood flow dynamics in human thoracic aorta, Comput. Methods Biomech. Biomed. Eng. 18 (2015) 1200–1216, https://doi.org/10.1080/10255842.2014.887698.

[28] S. Nadeem, N.S. Akbar, A.A. Hendi, T. Hayat, Power law fluid model for blood flow through a tapered artery with a stenosis, Appl. Math. Comput. 217 (2011) 7108–7116, https://doi.org/10.1016/j.amc.2011.01.026.

[29] B.M. Johnston, P.R. Johnston, S. Corney, D. Kilpatrick, Non-Newtonian blood flow in human right coronary arteries: steady state simulations, J. Biomech. 37 (2004) 709–720.

[30] S.-R. Yan, M. Zarringhalam, D. Toghraie, L.K. Foong, P. Talebizadehsardari, Numerical investigation of non-Newtonian blood flow within an artery with cone shape of stenosis in various stenosis angles, Comput. Methods Progr. Biomed. 192 (2020), 105434.

[31] A. Zaman, A.A. Khan, N. Ali, Modeling of unsteady non-Newtonian blood flow through a stenosed artery: with nanoparticles, J. Braz. Soc. Mech. Sci. Eng. 40 (2018) 1–12.

[32] B.P. Mahammod, E. Barua, A.B. Deoghare, K. Pandey, Permeability quantification of porous polymer scaffold for bone tissue engineering, Mater. Today Proc. 22 (2020) 1687–1693.

[33] D. Ali, S. Sen, Permeability and fluid flow-induced wall shear stress of bone tissue scaffolds: computational fluid dynamic analysis using Newtonian and non-Newtonian blood flow models, Comput. Biol. Med. 99 (2018) 201–208, https://doi.org/10.1016/j.compbiomed.2018.06.017.

[34] O. Al-Ketan, D.-W. Lee, R. Rowshan, R.K.A. Al-Rub, Functionally graded and multi-morphology sheet TPMS lattices: design, manufacturing, and mechanical properties, J. Mech. Behav. Biomed. Mater. 102 (2020), 103520, https://doi.org/10.1016/j.jmbbm.2019.103520.

[35] D. Mahmoud, K.S. Al-Rubaie, M.A. Elbestawi, The influence of selective laser melting defects on the fatigue properties of Ti6Al4V porosity graded gyroids for bone implants, Int. J. Mech. Sci. 193 (2021), 106180.

[36] D. Ali, S. Sen, Finite element analysis of mechanical behavior, permeability and fluid induced wall shear stress of high porosity scaffolds with gyroid and lattice-based architectures, J. Mech. Behav. Biomed. Mater. 75 (2017) 262–270, https://doi.org/10.1016/j.jmbbm.2017.07.035.

[37] Al-Ketan O, Abu Al-Rub RK. MSLattice: a free software for generating uniform and graded lattices based on triply periodic minimal surfaces. Mater. Des. Process. Commun. n.d.:e205.

[38] M.G. Bixel, A.P. Kusumbe, S.K. Ramasamy, K.K. Sivaraj, S. Butz, D. Vestweber, et al., Flow dynamics and HSPC homing in bone marrow microvessels, Cell Rep. 18 (2017) 1804–1816, https://doi.org/10.1016/j.celrep.2017.01.042.

[39] S. Gómez, M. Vlad, J. López, E. Fernández, Design and properties of 3D scaffolds for bone tissue engineering, Acta Biomater. 42 (2016) 341–350.

[40] T. Sochi, Non-Newtonian rheology in blood circulation, ArXiv Prepr (2013) 1–26. ArXiv13062067, https://arxiv.org/abs/1306.2067. ArXiv13062067.

[41] J. Boyd, J.M. Buick, S. Green, Analysis of the Casson and Carreau-Yasuda non-Newtonian blood models in steady and oscillatory flows using the lattice Boltzmann method, Phys. Fluids 19 (2007), 093103.

[42] J.Y. Park, D.H. Lee, E.J. Lee, S.-H. Lee, Study of cellular behaviors on concave and convex microstructures fabricated from elastic PDMS membranes, Lab Chip 9 (2009) 2043–2049.

[43] S.B. Blanquer, M. Werner, M. Hannula, S. Sharifi, G.P. Lajoinie, D. Eglin, et al., Surface curvature in triply-periodic minimal surface architectures as a distinct design parameter in preparing advanced tissue engineering scaffolds, Biofabrication 9 (2017), 025001, https://doi.org/10.1088/1758-5090/aa6553.

[44] S.J. Callens, R.J. Uyttendaele, L.E. Fratila-Apachitei, A.A. Zadpoor, Substrate curvature as a cue to guide spatiotemporal cell and tissue organization, Biomaterials 232 (2020), 119739, https://doi.org/10.1016/j.biomaterials.2019.119739.

[45] A. Jones, M. Leary, S. Bateman, M. Easton, Effect of surface geometry on laser powder bed fusion defects, J. Mater. Process. Technol. 296 (2021), 117179, https://doi.org/10.1016/j.jmatprotec.2021.117179.

[46] A.L. Mackay, Periodic minimal surfaces from finite element methods, Chem. Phys. Lett. 221 (1994) 317–321, https://doi.org/10.1016/0009-2614(94)00256-8.

[47] D.J. Whitehouse, Surfaces and Their Measurement, CRC Press, 2002.
[48] M. Chabanon, H. Duval, J. Grenier, C. Beauchesne, B. Goyeau, B. David, Histological method to study the effect of shear stress on cell proliferation and tissue morphology in a bioreactor, Tissue Eng. Regen Med. 16 (2019) 225–235.
[49] R. Asbai-Ghoudan, S. Ruiz de Galarreta, N. Rodriguez-Florez, Analytical model for the prediction of permeability of triply periodic minimal surfaces, J. Mech. Behav. Biomed. Mater. 124 (2021), 104804, https://doi.org/10.1016/j.jmbbm.2021.104804.